AIMS Mathematics, 11(5): 14984–15007.
DOI: 10.3934/math.2026616
Received: 14 April 2026
Revised: 18 May 2026
Accepted: 22 May 2026
Published: 28 May 2026

http://www.aimspress.com/journal/Math

*Research article*

# Deep learning for parameter estimation in a typhoid fever model

**Ramsha Shafqat**[1,*] **and Mohammed M. Alshamrani**[2]

[1] Department of Mathematics and Statistics, The University of Lahore, Sargodha 40100, Pakistan
[2] Department of Mathematics and Statistics, College of Science, Taif University, P.O. Box 11099, Taif 21944, Saudi Arabia

* **Correspondence:** Email: ramshawarriach@gnail.com.

**Abstract:** Typhoid fever remains a major public-health problem, particularly in regions with poor sanitation, unsafe water, and limited healthcare. Motivated by persistent transmission, treatment failure, and relapse, this study proposes a deterministic typhoid fever model with direct and environmental transmission, treatment, and relapse mechanisms. The model is formulated in the modified Atangana–Baleanu–Caputo (mABC) fractional framework to incorporate memory effects. Its main qualitative properties, including positivity, boundedness, existence, and uniqueness of solutions, are established. Numerically, the Laplace–Adomian decomposition method (LADM) is applied to obtain approximate solutions for different fractional orders. The results show that the fractional order strongly affects transient disease dynamics while preserving biologically meaningful behavior. A deep neural network (DNN) surrogate is also trained on the generated trajectories and assessed through standard diagnostics. In addition, parameter estimation is performed using clean and noisy synthetic data, showing good agreement between fitted and reference dynamics.

**Keywords:** typhoid fever; mABC fractional derivative; qualitative analysis; Laplace–Adomian decomposition; parameter estimation; model calibration; deep neural network
**Mathematics Subject Classification:** 34D20, 34K20, 34K60, 92C60, 92D45

## 1. Introduction

Caused by *Salmonella Typhi*, typhoid fever is a bacterial disease that is chiefly spread through contaminated food and drinking water [1, 2]. Although sanitation systems and public-health awareness have improved in many places, the disease continues to impose a considerable burden in developing areas where safe water, hygiene facilities, and healthcare services remain insufficient [3, 4]. Clinically, typhoid fever may present with prolonged fever, abdominal pain, headache, vomiting, diarrhea, and systemic complications, and if treatment is delayed, the infection

may become severe and life-threatening [5, 6]. For this reason, typhoid fever continues to attract considerable attention from epidemiologists, clinicians, and mathematical modelers.

Despite the routine use of antibiotics in typhoid treatment, the infection remains difficult to eliminate effectively. In some cases, symptoms may reappear when treatment is incomplete or when the clinical response is unsatisfactory [7, 8]. Moreover, a fraction of recovered individuals may continue to shed the bacteria for a long time, thereby sustaining disease transmission in the community [8, 9]. The growing problem of antimicrobial resistance further complicates treatment outcomes and reduces the overall effectiveness of standard control measures [10]. These features show that typhoid dynamics are influenced not only by infection and recovery, but also by treatment response, relapse behavior, and environmental persistence.

The study of infectious disease transmission and control has been greatly supported by mathematical modeling. For typhoid fever in particular, deterministic compartmental frameworks have been widely employed to investigate transmission routes, optimal intervention policies, forecasting behavior, and disease management strategies [3, 11]. Such models help to identify key epidemiological mechanisms and provide insight into the possible effects of treatment, sanitation, and vaccination policies [12, 13]. However, many classical models are formulated with integer-order derivatives, which describe only local interactions in time and may not adequately reflect memory-dependent biological processes.

In epidemic modeling, fractional calculus has attracted considerable attention because it extends classical differential equations by incorporating nonlocal memory and hereditary effects into the system dynamics [14, 15]. Compared with ordinary differential operators, fractional derivatives provide greater flexibility for describing disease evolution, delayed responses, and history-dependent transmission processes [16, 17]. Several recent studies have applied fractional-order methods to infectious-disease models, including typhoid-related systems, and have shown that the fractional order can significantly influence transient epidemic behavior [18]. This makes fractional modeling particularly suitable for diseases such as typhoid fever, where environmental contamination, treatment delay, carrier effects, and relapse may all contribute to memory-dependent dynamics. Recent contributions further demonstrate the usefulness of fractional operators in both epidemiological and nonlinear dynamical systems. For example, Ahmad et al. [19] investigated the global stability and computational behavior of a fractional HIV/AIDS epidemic model under the Caputo operator, while Ahmad et al. [20] analyzed norovirus transmission involving contaminated food and water. Beyond epidemiological applications, fractional operators have also been employed to study nonlinear physical systems, including soliton dynamics in fractional coupled Higgs systems and nonlinear spatiotemporal fractional quantum-mechanics equations [21, 22]. These studies highlight the effectiveness of fractional calculus in capturing memory effects, nonlinear interactions, and complex temporal behavior, thereby providing strong motivation for using the modified Atangana–Baleanu–Caputo (mABC) fractional framework in the present typhoid fever model. Recent studies have shown the importance of fractional calculus and machine-learning techniques in disease modeling. Al-Quran et al. [23] investigated a normalized Caputo–Fabrizio fractional model for ischemic heart disease progression, while Shafqat et al. [24] used fractional susceptible-infected-recovered-deceased (SIRD) dynamics with deep learning for epidemic prediction. Similar hybrid approaches have also been applied to rabies [25], Zika virus [26], and poliomyelitis dynamics [27]. These works highlight the effectiveness of fractional operators and learning-based methods in capturing memory effects and improving disease prediction.

The mABC operator is selected in this study because it combines a nonlocal fractional structure with a nonsingular Mittag–Leffler kernel. Unlike classical integer-order derivatives, which depend only on the instantaneous state of the system, the mABC derivative allows the present disease dynamics to depend on the previous history of infection, treatment, relapse, and environmental contamination. Compared with fractional operators with singular kernels, the nonsingular Mittag–Leffler kernel of the mABC operator provides a smoother memory representation and avoids kernel singularity at the initial time. This property is particularly suitable for typhoid fever dynamics, where bacterial persistence in the environment, delayed treatment response, carrier effects, and relapse after incomplete treatment are all history-dependent processes. Therefore, the mABC framework offers a biologically meaningful and mathematically flexible tool for describing memory-dependent transient epidemic behavior.

Beyond classical epidemic models, other nonlinear population-dynamics frameworks also provide useful mathematical insight into boundedness, transient behavior, and the role of nonlinear interactions. In particular, Keller–Segel-type chemotaxis models describe aggregation, attraction–repulsion effects, and spatio-temporal pattern formation in biological systems. Although these models arise in a different biological setting, they share conceptual similarities with epidemic models in which nonlinear interaction terms, nonlocal effects, and stability properties strongly influence the qualitative behavior of solutions. Recent studies on local and nonlocal attraction–repulsion chemotaxis models have shown how nonlinear dissipative mechanisms and combined production–consumption effects can prevent singular behavior and ensure boundedness [28, 29]. These contributions provide a broader mathematical background for the present work, where boundedness, positivity, memory effects, and transient disease dynamics are central parts of the analysis.

A number of studies have already investigated typhoid fever from different mathematical perspectives. Existing contributions include optimal control formulations, stochastic analyses, and fractional-order transmission models [11, 30]. Other works have employed techniques such as the differential transform method, Adomian decomposition, and related semi-analytical approaches to obtain approximate solutions of typhoid systems [31, 32]. Even so, the available literature still leaves room for improvement. In particular, many models do not simultaneously incorporate direct transmission, indirect environmental transmission, differentiated infectious classes, saturated treatment uptake, limited treatment efficacy, and relapse after treatment within a single fractional-order setting [11, 13]. Furthermore, only a limited number of studies combine rigorous mathematical analysis with modern data-driven approximation and calibration tools in the same framework.

Motivated by the preceding discussion, we propose a fractional-order typhoid fever model that describes the dynamics of susceptible, exposed, mildly infected, severely infected, carrier, treated, and recovered individuals, together with an environmental bacterial compartment. The formulation is established within the mABC framework, where the nonsingular Mittag–Leffler kernel makes it possible to account for memory-dependent effects in the transmission process [30]. We then analyze the principal mathematical properties of the system and prove positivity, boundedness, existence, and uniqueness of solutions, thereby ensuring that the model is both mathematically sound and biologically meaningful. An approximate recursive solution is subsequently constructed through the Laplace–Adomian decomposition method (LADM), and the resulting scheme is employed to investigate the influence of different fractional orders on the temporal behavior of the state variables.

Existing mathematical studies on typhoid fever have addressed several important aspects of disease transmission and control. For example, some works have focused on the impact of limited public-health resources and optimal intervention strategies, while others have developed forecasting and optimal-control frameworks for typhoid transmission dynamics [11, 30]. Fractional and stochastic formulations have also been proposed, including fractional co-infection models involving pneumonia and typhoid fever with cost-effective control measures, as well as fractional typhoid fever models incorporating mass-vaccination perspectives [11, 13]. These studies provide important theoretical and computational contributions; however, most of them focus mainly on vaccination, optimal control, stochastic effects, or general fractional transmission dynamics. In contrast, the present study develops a unified mABC fractional-order typhoid model that simultaneously incorporates direct human-to-human transmission, indirect environmental transmission, mildly infected, severely infected and carrier classes, saturated treatment uptake, limited treatment efficacy, relapse after treatment, and environmental bacterial persistence. Moreover, the proposed work goes beyond qualitative and numerical analysis by combining LADM-based approximation, DNN surrogate learning, and parameter calibration using both clean and noisy synthetic observations. Therefore, the present framework provides a more integrated analytical–computational approach for studying typhoid fever dynamics with treatment relapse and environmental contamination.

Beyond the theoretical and numerical analysis, the study also includes a data-driven stage. In particular, a DNN surrogate is built from the simulated trajectories to provide an efficient approximation of the system dynamics, while a parameter-calibration procedure is applied to estimate selected epidemiological quantities from both clean and noisy synthetic observations. In this way, the study does not stop at qualitative analysis alone, but also explores computational prediction and calibration aspects that are increasingly important in modern mathematical epidemiology.

The motivation of this paper comes from the need to better understand typhoid fever dynamics in situations where treatment is not fully effective, relapse may occur, and bacteria can persist in the environment. These mechanisms naturally suggest a memory-dependent formulation, which is more suitably described by a fractional operator than by a purely classical one. The novelty of the present study lies in developing a unified mABC typhoid modeling framework that incorporates direct and indirect transmission, explicit treatment and relapse pathways, qualitative well-posedness analysis, LADM-based numerical solutions, DNN-based surrogate modeling, and parameter calibration using both clean and noisy synthetic observations. Thus, the paper contributes not only a richer epidemic model, but also an integrated analytical–computational methodology for investigating typhoid fever transmission and treatment relapse. Based on the above motivation and identified research gap, we now formulate the proposed fractional-order typhoid fever model and describe its epidemiological compartments and transmission mechanisms.

## 2. Model formulation

This section develops a fractional-order compartmental model for typhoid fever that includes treatment, relapse, and environmental bacterial contamination. To capture memory-dependent effects that cannot be represented adequately by the classical integer-order setting, the model is formulated by means of the mABC derivative. In this way, nonlocal temporal interactions are incorporated without losing the biological meaning of the disease transitions. We denote the total human

population by $N_h(t) = S(t) + E(t) + I_m(t) + I_s(t) + I_c(t) + T(t) + R(t)$, where the compartments correspond to susceptible, exposed, mildly infected, severely infected, carrier, treated, and recovered individuals, respectively. The variable $B_c(t)$ is used for the bacterial load in the contaminated environment. Based on these compartments, the mABC typhoid fever model is formulated as follows:

$$\begin{cases} {}^{\text{mABC}}D_t^{\vartheta} S(t) = \Lambda - \lambda(t)S(t) - \mu S(t) + \sigma_2 R(t), \\ {}^{\text{mABC}}D_t^{\vartheta} E(t) = \lambda(t)S(t) - (\mu + \sigma)E(t), \\ {}^{\text{mABC}}D_t^{\vartheta} I_m(t) = p\sigma E(t) + \varpi_2(1-\theta_2)T(t) - (\mu + d_2 + \phi + \tau_3)I_m(t), \\ {}^{\text{mABC}}D_t^{\vartheta} I_s(t) = (1-p-q)\sigma E(t) + \phi I_m(t) - H(I_s(t)) - (\mu + d_1)I_s(t), \\ {}^{\text{mABC}}D_t^{\vartheta} I_c(t) = q\sigma E(t) + \tau_1 T(t) - (\mu + \tau_2)I_c(t), \\ {}^{\text{mABC}}D_t^{\vartheta} T(t) = H(I_s(t)) + \tau_3 I_m(t) + \tau_2 I_c(t) - (\mu + d_3 + \tau_1 + \sigma_1 + \varpi_2(1-\theta_2))T(t), \\ {}^{\text{mABC}}D_t^{\vartheta} R(t) = \sigma_1 T(t) - (\mu + \sigma_2)R(t), \\ {}^{\text{mABC}}D_t^{\vartheta} B_c(t) = \alpha B_c(t)\left(1 - \dfrac{B_c(t)}{K}\right) + \pi_1 I_s(t) + \pi_2 I_m(t) + \pi_3 I_c(t) - \mu_B B_c(t), \end{cases} \tag{2.1}$$

with the initial conditions $S(0) = N_1, E(0) = N_2, I_m(0) = N_3, I_s(0) = N_4, I_c(0) = N_5, T(0) = N_6, R(0) = N_7$, and $B_c(0) = N_8$. The parameters $\pi_1$, $\pi_2$, and $\pi_3$ denote the bacterial shedding rates from the severe infected, mild infected, and carrier classes, respectively. The parameter $\sigma_1$ represents the recovery rate from treatment, whereas $\sigma_2$ represents the loss of immunity rate from the recovered class to the susceptible class. In the saturated treatment function $H(I_s) = \frac{\theta_1 I_s}{1+\varpi_1 I_s}$, the parameter $\varpi_1$ denotes the treatment saturation coefficient. The parameter $\varpi_2$ is used only for the relapse-response term $\varpi_2(1-\theta_2)T$, where $\theta_2$ measures treatment efficacy. This notation is used consistently in all model equations, recurrence relations, parameter tables, and numerical simulations.

This function is nonnegative, increasing, and bounded, and it represents the fact that treatment demand rises with the number of severely infected individuals but eventually saturates because of limited treatment capacity. The force of infection is defined by $\lambda(t) = \frac{\beta_1\left(I_s(t)+\alpha_1 I_m(t)+\alpha_2 I_c(t)\right)}{N_h(t)} + \frac{\beta_2 B_c(t)}{K+B_c(t)}$. The first term describes direct human-to-human transmission, where severe, mild, and carrier infective individuals contribute differently to transmission. The second term represents indirect transmission through the bacteria-contaminated environment.

Figure 1 shows the compartmental organization of the model. The susceptible class gains individuals through recruitment at rate $\Lambda$ and through waning immunity from the recovered class at rate $\sigma_2$, while infection and natural mortality reduce its size. After infection, individuals enter the exposed class $E(t)$, remain there during the latent stage, and then progress at rate $\sigma$. From the exposed compartment, a proportion $p$ becomes mildly infected and enters $I_m(t)$, a proportion $1-p-q$ becomes severely infected and enters $I_s(t)$, and the rest, given by $q$, move into the carrier class $I_c(t)$. Mildly infected individuals may be treated at rate $\tau_3$, worsen to severe infection at rate $\phi$, or leave through natural and disease-related death. Severely infected individuals move to treatment according to $H(I_s)$ and may also experience disease-induced death at rate $d_1$. Treated individuals recover at rate $\sigma_1$, although incomplete treatment success can produce relapse. In particular, some re-enter the mild infection class at rate $\varpi_2(1-\theta_2)$, while others become carriers at rate $\tau_1$. Here, $\theta_2$ quantifies treatment efficacy, and lower values indicate weaker treatment performance and stronger relapse effects. The recovered compartment contains individuals who have successfully responded to treatment, but they may later lose immunity and move back into the susceptible class at rate $\sigma_2$.

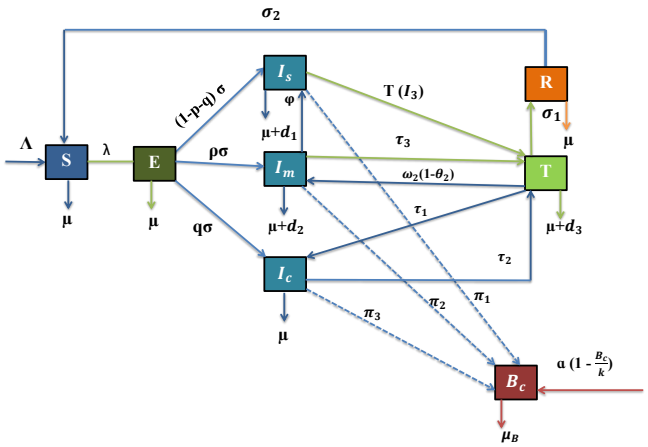


**Figure 1.** Schematic representation of the proposed typhoid fever model.

The environmental compartment $B_c(t)$ represents the bacterial load in contaminated surroundings. The environmental bacterial population follows logistic growth characterized by intrinsic rate $\alpha$ and carrying capacity $K$, while additional bacteria are introduced through shedding from the severe, mild, and carrier compartments at rates $\pi_1$, $\pi_2$, and $\pi_3$, respectively. The bacteria concentration decreases through natural removal at rate $\mu_B$. This environmental component enables the model to capture indirect transmission due to contaminated water, food, or unsanitary conditions. Therefore, the proposed model incorporates the principal epidemiological mechanisms of typhoid fever, namely direct transmission, indirect environmental transmission, treatment, relapse, carrier formation, and waning immunity, within a fractional-order framework. This formulation provides a more realistic basis for studying the effect of memory on typhoid fever dynamics. After presenting the biological structure of the model, we next introduce the fractional-calculus tools required for the subsequent mathematical analysis.

## 3. Auxiliary tools

We begin by presenting some standard results from fractional calculus that will be used later.

**Definition 3.1.** *[33] For a function $f \in L^1(0,T)$, the mABC derivative is defined by*

$$ {}^{\mathrm{mABC}}\mathbf{D}_t^{\vartheta} f(t) = \frac{\mathbf{M}(\vartheta)}{1-\vartheta}\left[ f(t) - \mathbf{E}_{\vartheta}(-\mu_{\vartheta} t^{\vartheta}) f(0) - \mu_{\vartheta} \int_0^t (t-u)^{\vartheta-1} \mathbf{E}_{\vartheta,\vartheta}(-\mu_{\vartheta}(t-u)^{\vartheta}) f(u)\, du \right]. \tag{3.1} $$

*Here, $\mathbf{E}_{\vartheta}$ denotes the one-parameter Mittag–Leffler function, whereas $\mathbf{E}_{\vartheta,\vartheta}$ denotes its two-parameter form. In particular, it follows from this definition that ${}^{\mathrm{mABC}}\mathbf{D}_t^{\vartheta} f = 0$.*

**Definition 3.2.** *[33] For $f \in L^1(0,T)$, the corresponding mABC integral operator is given by*

$$ {}^{\mathrm{mABC}}\mathbf{I}_0^{\vartheta} f = \frac{\mathbf{M}(1-\vartheta)}{\mathbf{M}(\vartheta)}[f(t) - f(0)] + \mu_{\vartheta}\left[ {}^{\mathrm{RL}}\mathbf{I}_0^{\vartheta}(f(t) - f(0)) \right]. \tag{3.2} $$

**Lemma 3.1.** *Let $f' \in L^1(0,\infty)$ and suppose that $\vartheta \in (0,1)$. Then one has*

$$ {}^{\mathrm{mABC}}\mathbf{I}_0^{\vartheta}\, {}^{\mathrm{mABC}}\mathbf{D}_0^{\vartheta} f(t) = f(t) - f(0). \tag{3.3} $$

In addition, the Laplace transform of the mABC derivative takes the form

$$\mathcal{L}\Big[{}^{\mathrm{mABC}}\mathbf{D}_0^{\vartheta} f(t); s\Big] = \frac{\mathbf{M}(\vartheta)}{1-\vartheta}\frac{s^{\vartheta}\mathcal{L}(f; s) - f(0)s^{\vartheta-1}}{s^{\vartheta}+\mu_{\vartheta}}, \qquad \left|\frac{\mu_{\vartheta}}{s^{\vartheta}}\right| < 1. \tag{3.4}$$

Using these preliminary definitions, we now examine the fundamental qualitative properties of the proposed system.

## 4. Qualitative analysis of the proposed model

In this section, we examine the main qualitative features of the proposed typhoid fever system governed by the mABC operator. For notational convenience, system (2) is rewritten in compact vector form as $X(t) = \big(S(t), E(t), I_m(t), I_s(t), I_c(t), T(t), R(t), B_c(t)\big)^{\top}$, with total human population $N_h(t) = S(t) + E(t) + I_m(t) + I_s(t) + I_c(t) + T(t) + R(t)$. To avoid ambiguity between the treated compartment $T(t)$ and the treatment response term, we denote the saturated treatment function by $\mathcal{H}(I_s) = \frac{\theta_1 I_s}{1+\varpi_1 I_s}$, which remains nonnegative, bounded, and increasing for $I_s \geq 0$. Furthermore, the force of infection is taken as $\lambda(t) = \frac{\beta_1\left(I_s+\alpha_1 I_m+\alpha_2 I_c\right)}{N_h(t)} + \frac{\beta_2 B_c}{K+B_c}$, so that the corresponding infection incidence is $\lambda(t)S(t)$.

Accordingly, the proposed model can be written as

$$\begin{cases} {}^{mABC}D_t^{\vartheta} S = \Lambda - \lambda S - \mu S + \sigma_2 R, \\ {}^{mABC}D_t^{\vartheta} E = \lambda S - (\mu+\sigma)E, \\ {}^{mABC}D_t^{\vartheta} I_m = p\sigma E + \varpi_2(1-\theta_2)T - (\mu+d_2+\phi+\tau_3)I_m, \\ {}^{mABC}D_t^{\vartheta} I_s = (1-p-q)\sigma E + \phi I_m - \mathcal{H}(I_s) - (\mu+d_1)I_s, \\ {}^{mABC}D_t^{\vartheta} I_c = q\sigma E + \tau_1 T - (\mu+\tau_2)I_c, \\ {}^{mABC}D_t^{\vartheta} T = \mathcal{H}(I_s) + \tau_3 I_m + \tau_2 I_c - (\mu+d_3+\tau_1+\sigma_1+\varpi_2(1-\theta_2))T, \\ {}^{mABC}D_t^{\vartheta} R = \sigma_1 T - (\mu+\sigma_2)R, \\ {}^{mABC}D_t^{\vartheta} B_c = \alpha B_c\left(1-\dfrac{B_c}{k}\right) + \pi_1 I_s + \pi_2 I_m + \pi_3 I_c - \mu_B B_c, \end{cases} \tag{4.1}$$

with the initial values $S(0) = N_1, E(0) = N_2, I_m(0) = N_3, I_s(0) = N_4, I_c(0) = N_5, T(0) = N_6, R(0) = N_7$, and $B_c(0) = N_8$, where $N_i \geq 0$ for $i = 1, \ldots, 8$. We consider the biologically feasible region $\Omega = \left\{X \in \mathbb{R}_+^8 : \ 0 \leq N_h(t) \leq \frac{\Lambda}{\mu}, \quad 0 \leq B_c(t) \leq M_B\right\}$, where $M_B > 0$ is a sufficiently large constant.

### 4.1. Positivity of solutions

**Theorem 4.1.** *Let $X(0) \in \mathbb{R}_+^8$. Then every solution of system* (4.1) *remains nonnegative for all $t \geq 0$. In other words, the nonnegative orthant $\mathbb{R}_+^8$ is positively invariant.*

*Proof.* We examine the right-hand side of each equation on the boundary of the nonnegative orthant. When $S = 0$, we have ${}^{mABC}D_t^{\vartheta} S\Big|_{S=0} = \Lambda + \sigma_2 R \geq 0$. When $E = 0$, it follows that ${}^{mABC}D_t^{\vartheta} E\Big|_{E=0} = \lambda S \geq 0$. When $I_m = 0$, one obtains ${}^{mABC}D_t^{\vartheta} I_m\Big|_{I_m=0} = p\sigma E + \varpi_2(1-\theta_2)T \geq 0$. When $I_s = 0$, since $\mathcal{H}(0) = 0$, we have ${}^{mABC}D_t^{\vartheta} I_s\Big|_{I_s=0} = (1-p-q)\sigma E + \phi I_m \geq 0$. When $I_c = 0$, ${}^{mABC}D_t^{\vartheta} I_c\Big|_{I_c=0} = q\sigma E + \tau_1 T \geq 0$.

When $T = 0$, ${}^{mABC}D_t^{\vartheta} T\Big|_{T=0} = \mathcal{H}(I_s) + \tau_3 I_m + \tau_2 I_c \geq 0$. When $R = 0$, ${}^{mABC}D_t^{\vartheta} R\Big|_{R=0} = \sigma_1 T \geq 0$. Finally, when $B_c = 0$, ${}^{mABC}D_t^{\vartheta} B_c\Big|_{B_c=0} = \pi_1 I_s + \pi_2 I_m + \pi_3 I_c \geq 0$. Thus, on each coordinate hyperplane, the fractional derivative points inward or is tangent to the boundary. By the fractional comparison principle, no trajectory starting in $\mathbb{R}^8_+$ can cross into the negative orthant. Hence, all state variables remain nonnegative for all $t \geq 0$. □

### *4.2. Boundedness and invariant region*

**Theorem 4.2.** *All solutions of system* (4.1) *with nonnegative initial conditions are uniformly bounded in* $\Omega$.

*Proof.* Summing the first seven equations of system (4.1), we obtain

$$ {}^{mABC}D_t^{\vartheta} N_h = \Lambda - \mu N_h - d_2 I_m - d_1 I_s - d_3 T \leq \Lambda - \mu N_h.$$

Applying the fractional comparison theorem gives

$$N_h(t) \leq N_h(0) E_{\vartheta}(-\mu t^{\vartheta}) + \Lambda \int_0^t (t-\xi)^{\vartheta-1} E_{\vartheta,\vartheta}(-\mu(t-\xi)^{\vartheta})\, d\xi.$$

Consequently,

$$0 \leq N_h(t) \leq \max\left\{N_h(0), \frac{\Lambda}{\mu}\right\}, \qquad t \geq 0.$$

Hence, the total human population is bounded.

Next, for the environmental bacteria concentration,

$$ {}^{mABC}D_t^{\vartheta} B_c = \alpha B_c\left(1 - \frac{B_c}{k}\right) + \pi_1 I_s + \pi_2 I_m + \pi_3 I_c - \mu_B B_c.$$

Using the boundedness of $N_h(t)$ and the nonnegativity of the infectious classes, we have

$$\pi_1 I_s + \pi_2 I_m + \pi_3 I_c \leq (\pi_1 + \pi_2 + \pi_3) N_h(t) \leq (\pi_1 + \pi_2 + \pi_3) \max\left\{N_h(0), \frac{\Lambda}{\mu}\right\}.$$

Therefore,

$$ {}^{mABC}D_t^{\vartheta} B_c \leq (\alpha - \mu_B) B_c - \frac{\alpha}{k} B_c^2 + (\pi_1 + \pi_2 + \pi_3) \max\left\{N_h(0), \frac{\Lambda}{\mu}\right\}.$$

The right-hand side is a logistic-type upper bound, and thus $B_c(t)$ remains bounded for all $t \geq 0$. Hence, every solution enters and remains in the positively invariant bounded set $\Omega$. □

### *4.3. Existence and uniqueness of solutions*

Let $\mathcal{X} = C([0,T], \mathbb{R}^8)$ equipped with the norm $\|X\|_{\infty} = \max_{t\in[0,T]} \sum_{i=1}^{8} |X_i(t)|$. Denote by $F(t,X)$ the vector field associated with system (4.1). By the mABC integral operator, system (4.1) is equivalent to the integral equation

$$X(t) = X_0 + \frac{1-\vartheta}{M(\vartheta)} F(t, X(t)) + \frac{\vartheta}{M(\vartheta)\Gamma(\vartheta)} \int_0^t (t-\xi)^{\vartheta-1} F(\xi, X(\xi))\, d\xi. \tag{4.2}$$

**Theorem 4.3.** *Assume that $F : [0,T] \times \Omega \to \mathbb{R}^8$ is continuous and Lipschitz continuous with respect to $X$ on $\Omega$; that is, there exists $L > 0$ such that $\|F(t,X) - F(t,Y)\| \le L\|X - Y\|$, $X, Y \in \Omega$, $t \in [0,T]$. If*

$$\kappa := \frac{(1-\vartheta)L}{M(\vartheta)} + \frac{L\,T^{\vartheta}}{M(\vartheta)\Gamma(\vartheta+1)} < 1, \tag{4.3}$$

*then system* (4.1) *admits a unique solution on* $[0,T]$.

*Proof.* Define the operator $\mathcal{F} : \mathcal{X} \to \mathcal{X}$ by

$$(\mathcal{F}X)(t) = X_0 + \frac{1-\vartheta}{M(\vartheta)}F(t,X(t)) + \frac{\vartheta}{M(\vartheta)\Gamma(\vartheta)}\int_0^t (t-\xi)^{\vartheta-1}F(\xi,X(\xi))\,d\xi.$$

For $X, Y \in \mathcal{X}$,

$$\begin{aligned}\|(\mathcal{F}X)(t) - (\mathcal{F}Y)(t)\| \le{}& \frac{1-\vartheta}{M(\vartheta)}\|F(t,X(t)) - F(t,Y(t))\| \\ &+ \frac{\vartheta}{M(\vartheta)\Gamma(\vartheta)}\int_0^t (t-\xi)^{\vartheta-1}\|F(\xi,X(\xi)) - F(\xi,Y(\xi))\|\,d\xi.\end{aligned}$$

Using the Lipschitz condition yields

$$\|(\mathcal{F}X)(t) - (\mathcal{F}Y)(t)\| \le \frac{(1-\vartheta)L}{M(\vartheta)}\|X - Y\|_\infty + \frac{\vartheta L}{M(\vartheta)\Gamma(\vartheta)}\int_0^t (t-\xi)^{\vartheta-1}\,d\xi\,\|X - Y\|_\infty.$$

Since $\int_0^t (t-\xi)^{\vartheta-1}\,d\xi = \frac{t^\vartheta}{\vartheta}$, we obtain

$$\|\mathcal{F}X - \mathcal{F}Y\|_\infty \le \left[\frac{(1-\vartheta)L}{M(\vartheta)} + \frac{L\,T^{\vartheta}}{M(\vartheta)\Gamma(\vartheta+1)}\right]\|X - Y\|_\infty = \kappa\|X - Y\|_\infty.$$

Condition (4.3) implies that $\mathcal{F}$ is a contraction. Hence, by Banach's fixed-point theorem, $\mathcal{F}$ has a unique fixed point in $\mathcal{X}$, which is the unique solution of system (4.1) on $[0,T]$. □

**Remark 4.4.** *Since the nonlinear incidence and treatment functions are smooth on $\Omega$, the vector field $F$ is locally Lipschitz on the positively invariant bounded region established above. Therefore, the previous theorem applies on every finite interval* $[0,T]$.

## 5. Approximate solution by the Laplace–Adomian decomposition method

In this section, we derive a recursive approximation for system (4.1) by means of the LADM. The method is carried out directly on the full nonlinear typhoid fever model and treats the nonlinear incidence, the saturated treatment term, and the environmental logistic contribution through Adomian polynomials.

### *5.1. Integral form suitable for decomposition*

For any sufficiently smooth function $f$, define the fractional integral-type operator

$$\Phi_\vartheta[f](t) = \frac{1-\vartheta}{M(\vartheta)}f(t) + \frac{\vartheta}{M(\vartheta)\Gamma(\vartheta)}\int_0^t (t-\xi)^{\vartheta-1}f(\xi)\,d\xi.$$

Then, the mABC system (4.1) can be written as

$$X(t) = X_0 + \Phi_\vartheta(F(\cdot, X(\cdot)))(t). \tag{5.1}$$

To simplify the nonlinear terms, we introduce $\mathcal{I}(S, I_m, I_s, I_c, B_c) = \left(\frac{\beta_1\left(I_s+\alpha_1 I_m+\alpha_2 I_c\right)}{N_h} + \frac{\beta_2 B_c}{K+B_c}\right)S$, $\mathcal{H}(I_s) = \frac{\theta_1 I_s}{1+\varpi_1 I_s}$, and $\mathcal{G}(B_c) = B_c\left(1 - \frac{B_c}{k}\right)$. Hence, system (4.1) becomes

$$\begin{cases} S = N_1 + \Phi_\vartheta[\Lambda - \mathcal{I} - \mu S + \sigma_2 R], \\ E = N_2 + \Phi_\vartheta[\mathcal{I} - (\mu+\sigma)E], \\ I_m = N_3 + \Phi_\vartheta[p\sigma E + \varpi_2(1-\theta_2)T - (\mu + d_2 + \phi + \tau_3)I_m], \\ I_s = N_4 + \Phi_\vartheta[(1-p-q)\sigma E + \phi I_m - \mathcal{H}(I_s) - (\mu + d_1)I_s], \\ I_c = N_5 + \Phi_\vartheta[q\sigma E + \tau_1 T - (\mu+\tau_2)I_c], \\ T = N_6 + \Phi_\vartheta[\mathcal{H}(I_s) + \tau_3 I_m + \tau_2 I_c - (\mu + d_3 + \tau_1 + \sigma_1 + \varpi_2(1-\theta_2))T], \\ R = N_7 + \Phi_\vartheta[\sigma_1 T - (\mu+\sigma_2)R], \\ B_c = N_8 + \Phi_\vartheta[\alpha\mathcal{G}(B_c) + \pi_1 I_s + \pi_2 I_m + \pi_3 I_c - \mu_B B_c]. \end{cases} \tag{5.2}$$

### 5.2. Adomian decomposition

We seek the solution in the series form

$$S(t) = \sum_{n=0}^{\infty} S_n(t), \quad E(t) = \sum_{n=0}^{\infty} E_n(t), \quad I_m(t) = \sum_{n=0}^{\infty} I_{m,n}(t), \quad I_s(t) = \sum_{n=0}^{\infty} I_{s,n}(t),$$

$$I_c(t) = \sum_{n=0}^{\infty} I_{c,n}(t), \quad T(t) = \sum_{n=0}^{\infty} T_n(t), \quad R(t) = \sum_{n=0}^{\infty} R_n(t), \quad B_c(t) = \sum_{n=0}^{\infty} B_{c,n}(t).$$

The nonlinear terms are expanded as

$$\mathcal{I} = \sum_{n=0}^{\infty} \mathcal{A}_n, \qquad \mathcal{H}(I_s) = \sum_{n=0}^{\infty} \mathcal{B}_n, \qquad \mathcal{G}(B_c) = \sum_{n=0}^{\infty} C_n,$$

where the Adomian polynomials are defined by

$$\mathcal{A}_n = \frac{1}{n!}\frac{d^n}{dp^n}\left[\mathcal{I}\left(\sum_{k=0}^{\infty} p^k S_k, \sum_{k=0}^{\infty} p^k I_{m,k}, \sum_{k=0}^{\infty} p^k I_{s,k}, \sum_{k=0}^{\infty} p^k I_{c,k}, \sum_{k=0}^{\infty} p^k B_{c,k}\right)\right]_{p=0},$$

$$\mathcal{B}_n = \frac{1}{n!}\frac{d^n}{dp^n}\left[\frac{\theta_1 \sum_{k=0}^{\infty} p^k I_{s,k}}{1 + \varpi_1 \sum_{k=0}^{\infty} p^k I_{s,k}}\right]_{p=0}, \quad C_n = \frac{1}{n!}\frac{d^n}{dp^n}\left[\left(\sum_{k=0}^{\infty} p^k B_{c,k}\right)\left(1 - \frac{1}{k}\sum_{k=0}^{\infty} p^k B_{c,k}\right)\right]_{p=0}.$$

The first few Adomian polynomials needed in practice are $\mathcal{B}_0 = \frac{\theta_1 I_{s,0}}{1+\varpi_1 I_{s,0}}$, $\mathcal{B}_1 = \frac{\theta_1 I_{s,1}}{(1+\varpi_1 I_{s,0})^2}$, and $C_0 = B_{c,0}\left(1 - \frac{B_{c,0}}{k}\right)$, $C_1 = B_{c,1}\left(1 - \frac{2B_{c,0}}{k}\right)$. The polynomial $\mathcal{A}_0$ is simply the incidence function evaluated at the zeroth components,

$$\mathcal{A}_0 = \left(\frac{\beta_1(I_{s,0} + \alpha_1 I_{m,0} + \alpha_2 I_{c,0})}{N_{h,0}} + \frac{\beta_2 B_{c,0}}{K + B_{c,0}}\right)S_0,$$

where $N_{h,0} = S_0 + E_0 + I_{m,0} + I_{s,0} + I_{c,0} + T_0 + R_0$.

### 5.3. Recursive scheme

Substituting the series expansions into (5.2) and comparing like terms gives the following recurrence relations.

The zeroth-order components are the initial data: $S_0 = N_1, E_0 = N_2, I_{m,0} = N_3, I_{s,0} = N_4, I_{c,0} = N_5, T_0 = N_6, R_0 = N_7$, and $B_{c,0} = N_8$. For $n \geq 0$, the higher-order terms are obtained recursively from

$$\begin{cases} S_{n+1} = \Phi_\vartheta[\Lambda - \mathcal{A}_n - \mu S_n + \sigma_2 R_n], \\ E_{n+1} = \Phi_\vartheta[\mathcal{A}_n - (\mu + \sigma)E_n], \\ I_{m,n+1} = \Phi_\vartheta[p\sigma E_n + \varpi_2(1-\theta_2)T_n - (\mu + d_2 + \phi + \tau_3)I_{m,n}], \\ I_{s,n+1} = \Phi_\vartheta[(1-p-q)\sigma E_n + \phi I_{m,n} - \mathcal{B}_n - (\mu + d_1)I_{s,n}], \\ I_{c,n+1} = \Phi_\vartheta[q\sigma E_n + \tau_1 T_n - (\mu + \tau_2)I_{c,n}], \\ T_{n+1} = \Phi_\vartheta[\mathcal{B}_n + \tau_3 I_{m,n} + \tau_2 I_{c,n} - (\mu + d_3 + \tau_1 + \sigma_1 + \varpi_2(1-\theta_2))T_n], \\ R_{n+1} = \Phi_\vartheta[\sigma_1 T_n - (\mu + \sigma_2)R_n], \\ B_{c,n+1} = \Phi_\vartheta[\alpha C_n + \pi_1 I_{s,n} + \pi_2 I_{m,n} + \pi_3 I_{c,n} - \mu_B B_{c,n}]. \end{cases} \tag{5.3}$$

Consequently, the truncated $m$-term LADM approximation is

$$S^{(m)}(t) = \sum_{n=0}^{m} S_n(t), E^{(m)}(t) = \sum_{n=0}^{m} E_n(t), I_m^{(m)}(t) = \sum_{n=0}^{m} I_{m,n}(t), I_s^{(m)}(t) = \sum_{n=0}^{m} I_{s,n}(t),$$
$$I_c^{(m)}(t) = \sum_{n=0}^{m} I_{c,n}(t), T^{(m)}(t) = \sum_{n=0}^{m} T_n(t), R^{(m)}(t) = \sum_{n=0}^{m} R_n(t), B_c^{(m)}(t) = \sum_{n=0}^{m} B_{c,n}(t).$$

Using (5.3), the first-order components are

$$\begin{aligned} S_1 &= \Phi_\vartheta[\Lambda - \mathcal{A}_0 - \mu S_0 + \sigma_2 R_0], \\ E_1 &= \Phi_\vartheta[\mathcal{A}_0 - (\mu + \sigma)E_0], \\ I_{m,1} &= \Phi_\vartheta[p\sigma E_0 + \varpi_2(1-\theta_2)T_0 - (\mu + d_2 + \phi + \tau_3)I_{m,0}], \\ I_{s,1} &= \Phi_\vartheta[(1-p-q)\sigma E_0 + \phi I_{m,0} - \mathcal{B}_0 - (\mu + d_1)I_{s,0}], \\ I_{c,1} &= \Phi_\vartheta[q\sigma E_0 + \tau_1 T_0 - (\mu + \tau_2)I_{c,0}], \\ T_1 &= \Phi_\vartheta[\mathcal{B}_0 + \tau_3 I_{m,0} + \tau_2 I_{c,0} - (\mu + d_3 + \tau_1 + \sigma_1 + \varpi_2(1-\theta_2))T_0], \\ R_1 &= \Phi_\vartheta[\sigma_1 T_0 - (\mu + \sigma_2)R_0], \\ B_{c,1} &= \Phi_\vartheta[\alpha C_0 + \pi_1 I_{s,0} + \pi_2 I_{m,0} + \pi_3 I_{c,0} - \mu_B B_{c,0}]. \end{aligned}$$

Similarly, the second-order terms are

$$\begin{aligned} S_2 &= \Phi_\vartheta[\Lambda - \mathcal{A}_1 - \mu S_1 + \sigma_2 R_1], \\ E_2 &= \Phi_\vartheta[\mathcal{A}_1 - (\mu + \sigma)E_1], \\ I_{m,2} &= \Phi_\vartheta[p\sigma E_1 + \varpi_2(1-\theta_2)T_1 - (\mu + d_2 + \phi + \tau_3)I_{m,1}], \\ I_{s,2} &= \Phi_\vartheta[(1-p-q)\sigma E_1 + \phi I_{m,1} - \mathcal{B}_1 - (\mu + d_1)I_{s,1}], \\ I_{c,2} &= \Phi_\vartheta[q\sigma E_1 + \tau_1 T_1 - (\mu + \tau_2)I_{c,1}], \\ T_2 &= \Phi_\vartheta[\mathcal{B}_1 + \tau_3 I_{m,1} + \tau_2 I_{c,1} - (\mu + d_3 + \tau_1 + \sigma_1 + \varpi_2(1-\theta_2))T_1], \end{aligned}$$

$$
\begin{aligned}
R_2 &= \Phi_\vartheta[\sigma_1 T_1 - (\mu + \sigma_2) R_1], \\
B_{c,2} &= \Phi_\vartheta[\alpha C_1 + \pi_1 I_{s,1} + \pi_2 I_{m,1} + \pi_3 I_{c,1} - \mu_B B_{c,1}].
\end{aligned}
$$

Hence, the approximate series solution of the proposed typhoid model is given by $X(t) \approx X^{(m)}(t) = \sum_{n=0}^{m} X_n(t)$, for a sufficiently large truncation index $m$.

### *5.4. Convergence of the decomposition series*

**Theorem 5.1.** *Let $F$ satisfy the contractive condition given in* (4.3)*. Then the decomposition series generated by* (5.3) *converges uniformly on* $[0, T]$ *to the unique solution of system* (4.1)*.*

*Proof.* The recursive construction (5.3) is obtained from the fixed-point equation (5.1). Since the associated operator is a contraction under condition (4.3), the Picard sequence converges uniformly to the unique fixed point. The LADM components represent successive correction terms of the same operator, and therefore the partial sums converge to the unique solution of the original system. □

In practice, the truncated approximation $X^{(m)}(t)$ is used for numerical simulations, and the iteration is stopped once $\max_{t\in[0,T]} \|X^{(m+1)}(t) - X^{(m)}(t)\| < \varepsilon$ for a prescribed tolerance $\varepsilon > 0$. After establishing the well-posedness and deriving the approximate solution scheme, we now investigate the numerical behavior of the proposed model.

## 6. Numerical simulation

This section examines the numerical dynamics of the proposed typhoid fever model governed by the mABC fractional operator. To obtain the trajectories of the state variables, we employ the recursive approximation developed in Section 4 and evaluate the model for several fractional-order values. The numerical simulations are carried out by using the parameter set and initial conditions listed in Table 1, namely $S(0) = 10000$, $E(0) = 300$, $I_m(0) = 100$, $I_s(0) = 10$, $I_c(0) = 10$, $T(0) = 100$, $R(0) = 0$, and $B_c(0) = 100000$. To investigate the role of memory effects in the epidemic dynamics, we consider the fractional orders $\vartheta = 0.80, 0.85, 0.90, 0.95$, and we interpret the limiting case $\vartheta = 1$ as the corresponding classical integer-order model. These values allow us to compare the effect of weaker and stronger memory on the temporal evolution of all model compartments.

**Table 1.** Comparison between true and estimated parameter values, along with absolute and percentage errors.

| Parameter | True Value | Estimated Value | Absolute Error | Percent Error (%) |
|---|---|---|---|---|
| $\beta_1$ | $5.0 \times 10^{-5}$ | 0.0087224 | 0.0086724 | 17345.0 |
| $\beta_2$ | 0.0007 | 0.00015202 | 0.00054798 | 78.282 |
| $\tau_3$ | 0.65 | 0.5202 | 0.1298 | 19.969 |
| $\theta_2$ | 0.50 | 0.6481 | 0.1481 | 29.620 |
| $\omega_2$ | 0.56 | 0.35006 | 0.20994 | 37.490 |
| $E_0$ | 300 | 373.89 | 73.886 | 24.629 |
| $B_{c0}$ | $1.0 \times 10^5$ | $1.5967 \times 10^5$ | 59671 | 59.671 |

Some parameters in Table 2 are marked as assumed because direct typhoid-specific empirical estimates are not available for all epidemiological, treatment, relapse, and environmental mechanisms considered in the proposed model. These assumed values are not intended to represent fixed universal constants; rather, they are used as biologically admissible baseline values for numerical simulation. They were chosen to remain positive, to satisfy the feasible-region assumptions of the model, and to generate epidemiologically meaningful trajectories consistent with the qualitative properties proved above. To reduce the uncertainty associated with these assumed quantities, the most influential transmission- and treatment-related parameters, namely $\beta_1, \beta_2, \tau_3, \theta_2, \varpi_2, E(0)$, and $B_c(0)$, are further examined through the parameter-estimation procedure using both clean and noisy synthetic data. Therefore, the assumed values provide a baseline scenario, while the calibration results help evaluate the influence and recoverability of key parameters on the model output.

**Table 2.** Parameters and their numerical values in model 2.1.

| Notation | Value | Source | Notation | Value | Source | Notation | Value | Source |
|---|---|---|---|---|---|---|---|---|
| $\Lambda$ | 100 | [3] | $\sigma_2$ | 0.000904 | [34] | $\phi$ | 0.04 | Assumed |
| $\alpha$ | 0.014 | [35] | $p, q$ | [0,1] | Assumed | $\tau_3$ | 0.65 | Assumed |
| $\mu$ | 0.00005 | [8] | $d_1$ | 0.12 | [36] | $d_3$ | 0.015 | [8] |
| $d_2$ | 0.004 | Assumed | $\pi_1$ | 0.7 | [3] | $\pi_2$ | 0.8 | Assumed |
| $\pi_3$ | 0.9 | [37] | $\mu_B$ | 0.0345 | [35] | $\beta_1$ | 0.00005 | Assumed |
| $\tau_1$ | 0.055 | Assumed | $\beta_2$ | 0.0007 | Assumed | $K$ | 500000 | [37] |
| $\theta_1$ | 0.2827 | [38] | $\theta_2$ | 0.5 | Assumed | $\varpi_2$ | 0.56 | Assumed |
| $\varpi_1$ | 0.62 | [30] | $\alpha_1$ | 0.6 | [37] | $\alpha_2$ | 1.2 | [37] |
| $\sigma$ | 0.0556 | [38] | $\tau_2$ | 0.2 | Assumed | S(0) | 10000 | Assumed |

Figure 2 presents the simulated trajectories of the proposed system for the chosen fractional-order values. As displayed in Figure 2(a), the susceptible class declines steadily with time, reflecting the continued movement of individuals into infection through both direct contact and environmental transmission. The exposed class in Figure 2(b) first increases, reaches a peak, and then exhibits a slight decline, reflecting the transient accumulation of newly infected individuals before they progress to the infectious stages. In Figure 2(c), the mildly infected class initially decreases slightly and then rises gradually, indicating the combined influence of disease progression, treatment, and relapse effects. Figures 2(d)–2(f) display the temporal behavior of the severe infected, carrier, and treated classes, respectively. These profiles show that the disease burden is redistributed among clinically different infectious groups as the epidemic evolves. In particular, the treated class increases with time, which is compatible with the transfer of infected individuals into treatment. Figure 2(g) demonstrates the monotone increase of the recovered population due to successful treatment, while Figure 2(h) shows the growth of the bacteria-contaminated environment caused by bacterial shedding from infected individuals together with environmental persistence. Overall, the trajectories remain smooth, nonnegative, and biologically meaningful for all tested fractional orders, which agrees with the positivity and boundedness results established in the qualitative analysis.

Although the simulations in Figure 2 are presented for fractional orders $\vartheta = 0.80, 0.85, 0.90, 0.95$, it is important to relate these results to the classical integer-order model. The limiting case $\vartheta = 1$ corresponds to the standard memory-free formulation, in which the future evolution depends only on

the current state of the system. In contrast, when $\vartheta < 1$, the mABC operator incorporates nonlocal memory effects through the Mittag–Leffler kernel. Therefore, the fractional-order parameter acts as a memory index that controls the speed and intensity of the transient epidemic response. Compared with the integer-order case, smaller values of $\vartheta$ allow delayed and history-dependent changes in the susceptible, infected, treated, recovered, and environmental bacterial compartments. This is particularly relevant for typhoid fever because environmental contamination, treatment delay, carrier effects, and relapse are processes that may depend on previous disease history. Hence, the fractional-order formulation provides additional modeling flexibility beyond the classical integer-order model, especially in describing transient disease dynamics.

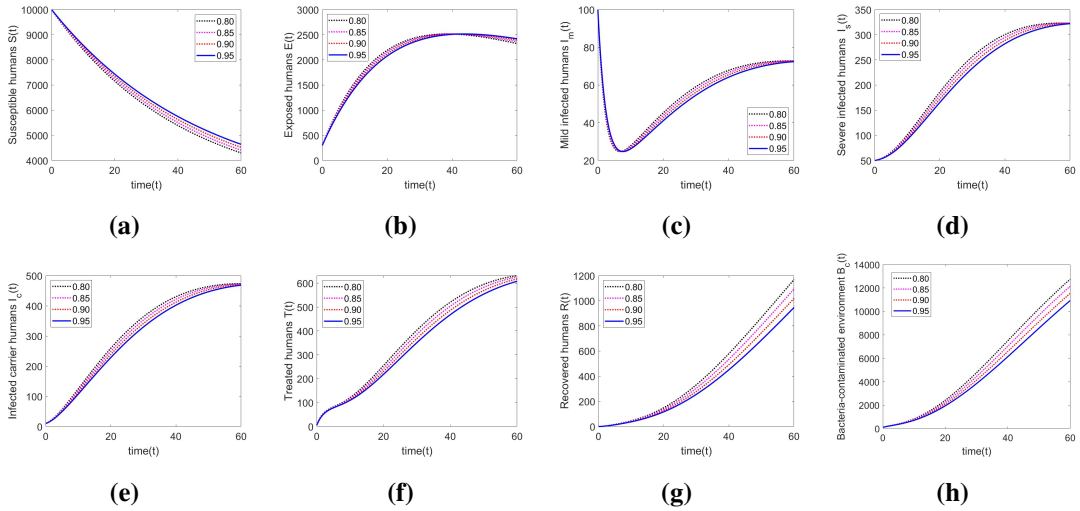


**Figure 2.** State trajectories of the proposed typhoid fever system for $\vartheta = 0.80, 0.85, 0.90, 0.95$: (a) $S(t)$, (b) $E(t)$, (c) $I_m(t)$, (d) $I_s(t)$, (e) $I_c(t)$, (f) $T(t)$, (g) $R(t)$, and (h) $B_c(t)$.

The simulations further indicate that the fractional order has a clear influence on the transient behavior of the system. Although the qualitative pattern of each compartment remains unchanged, the speed of increase or decrease and the corresponding population levels vary with $\vartheta$. This confirms that the modified fractional operator introduces a memory effect into the model, allowing the dynamics to capture nonlocal temporal dependence that cannot be represented by the classical integer-order framework. Hence, the fractional-order formulation provides additional flexibility in describing the spread of typhoid fever and the interaction between infection, treatment, relapse, and environmental contamination.

To support the data-driven component of the study, the numerically generated solutions are also used to train a DNN surrogate model. The purpose of this surrogate is to learn the relationship between the model inputs and the corresponding state trajectories, thereby reducing the computational cost of repeated simulations. For reproducibility, the DNN architecture is described as follows. The input layer consists of the time variable and the fractional-order value, while the output layer predicts the state variables $S(t), E(t), I_m(t), I_s(t), I_c(t), T(t), R(t)$, and $B_c(t)$. The network is constructed as a feed-forward DNN with four hidden layers containing 50, 30, 20, and 10 neurons, respectively. Hyperbolic tangent sigmoid activation functions are used in the hidden layers, and a linear activation function is

used in the output layer. The training data are generated from the LADM numerical solutions of the proposed mABC typhoid model for different fractional orders. The dataset is divided into training, validation, and testing subsets to evaluate the learning accuracy and generalization performance of the network. In the present study, a single DNN is trained for all state variables and all fractional orders.

The training performance and diagnostic results are presented in Figure 3. Figure 3(a) displays the mean squared error curves for the training, validation, and testing datasets. The three curves decrease rapidly and remain close to one another, indicating stable learning and good generalization. The best validation performance is achieved at epoch 200, with a value on the order of $10^{-8}$, which confirms the high predictive accuracy of the network. Figure 3(b) shows the gradient, damping parameter, and validation checks during training, all of which indicate a stable convergence behavior of the optimization procedure.

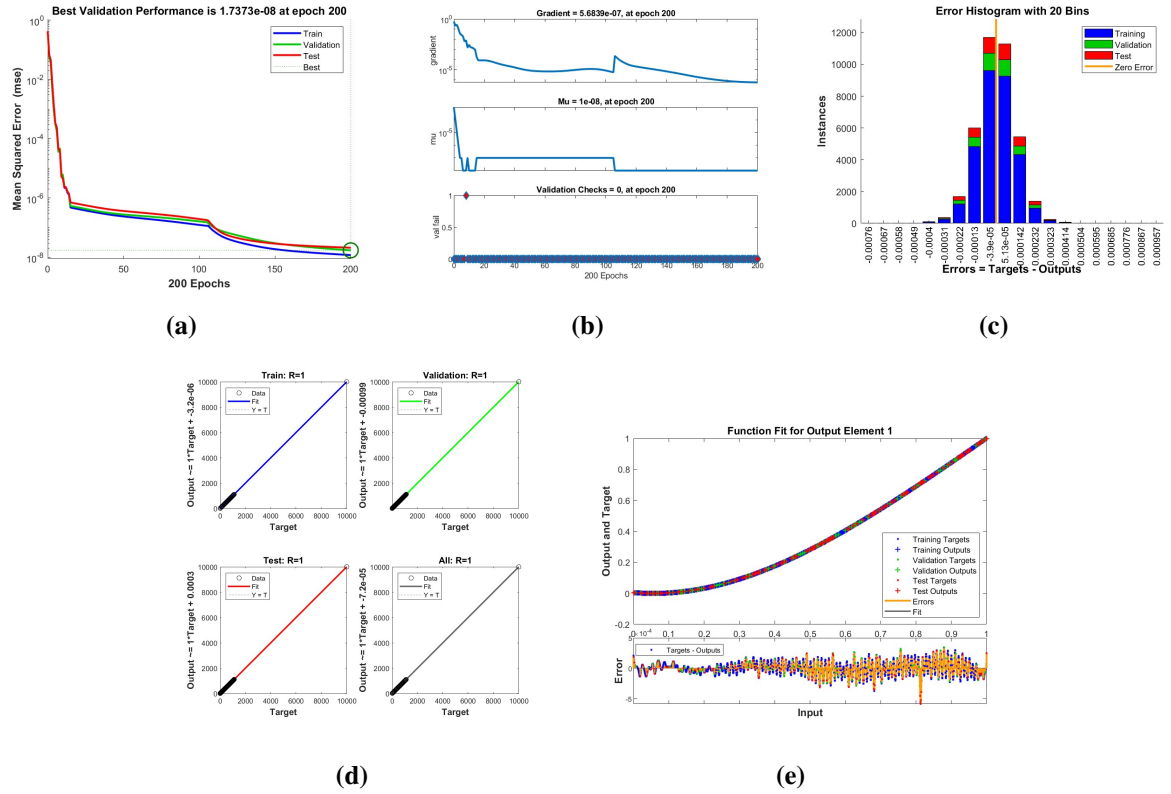


**Figure 3.** DNN performance and training diagnostics for the proposed typhoid fever model: (a) mean squared error curves for the training, validation, and testing sets, (b) gradient, damping parameter $\mu$, and validation checks versus epochs, (c) error histogram, (d) regression plots for training, validation, testing, and overall data, and (e) function fitting together with residual errors.

Figure 3(c) presents the error histogram, where the residuals are concentrated near zero, showing that the prediction errors are small and well controlled. The regression plots in Figure 3(d) demonstrate an excellent agreement between the network outputs and the target values for the training, validation, testing, and overall datasets, with the fitted lines lying very close to the ideal regression line. Finally, Figure 3(e) shows the function fitting and residual behavior, further confirming that the trained network

accurately reproduces the numerical solutions of the proposed fractional typhoid model.

To further clarify the practical role of the DNN surrogate, we compared its computational cost with that of the LADM approximation. The LADM scheme serves as the reference numerical method and is used to generate the training trajectories. However, for each new simulation setting, LADM requires recursive construction and evaluation of the decomposition terms. In contrast, once the DNN has been trained, prediction is obtained through direct forward propagation, which is computationally inexpensive. Therefore, the DNN is not intended to replace LADM in the theoretical construction of the solution; rather, it provides a fast surrogate model for repeated simulations, parameter screening, calibration loops, and uncertainty analysis. This is particularly useful when many trajectories must be evaluated for different fractional orders or parameter values. The numerical experiments and the deep learning diagnostics together verify that the proposed model is capable of producing stable and biologically consistent dynamics, while the neural network surrogate provides an efficient and accurate computational tool for approximation, calibration, and further predictive analysis. Having analyzed the numerical trajectories and the performance of the DNN surrogate, we next examine the parameter-estimation problem using synthetic data.

## 7. Parameter estimation

The proposed typhoid fever model captures the essential mechanisms of direct transmission, environmental contamination, treatment, and relapse, thus several parameters in Table 2 are assumed rather than directly measured. For this reason, parameter estimation is performed in order to improve the quantitative reliability of the model and to assess how well the model can recover important epidemiological quantities from trajectory data. In this section, we calibrate a biologically meaningful subset of the model parameters while keeping the remaining parameters fixed at the baseline values reported in Table 2.

Let $y_i$, $i = 1, 2, \ldots, n$ denote the available observed data collected at times $0 < t_1 < t_2 < \cdots < t_n$. Since the present study is based on model-generated trajectories, we consider synthetic observations constructed from the numerical solution of the proposed system. To connect the data with the epidemic dynamics, we use the model states directly and calibrate the system by minimizing the discrepancy between the observed trajectories and the model-predicted trajectories over the observation window. In particular, we estimate the parameter vector $\Theta = (\beta_1, \beta_2, \tau_3, \theta_2, \varpi_2, E(0), B_c(0))$, where $\beta_1$ and $\beta_2$ are the direct and indirect transmission rates, $\tau_3$ is the treatment rate of mildly infected individuals, $\theta_2$ measures the limited clinical efficacy of antibiotics, $\varpi_2$ denotes the relapse response after treatment, and $E(0)$ and $B_c(0)$ represent the initial exposed population and the initial bacteria concentration in the environment, respectively.

The unknown vector $\Theta$ is obtained by solving a nonlinear least-squares optimization problem of the form $\Theta^* = \arg\min_{\Theta\in\Omega} J(\Theta)$, where $J(\Theta) = \sum_{i=1}^{n} \|X(t_i;\Theta) - Y_i\|^2$. Here, $X(t_i;\Theta)$ denotes the model-predicted state vector at time $t_i$, $Y_i$ denotes the corresponding observed or synthetic data vector, and $\Omega$ is the biologically admissible parameter region. In the present study, the admissible set is chosen as $\beta_1 > 0, \beta_2 > 0, 0 < \tau_3 < 1, 0 < \theta_2 < 1, \varpi_2 > 0, E(0) \geq 0$, and $B_c(0) \geq 0$. These constraints ensure that the estimated quantities remain epidemiologically meaningful throughout the calibration process.

To evaluate the robustness of the fitting procedure, two calibration settings are considered. In the first setting, the model is fitted to clean synthetic trajectories generated from the proposed

fractional-order system. In the second setting, noisy synthetic observations are used in order to mimic measurement uncertainty and report variability that typically arise in epidemiological data. This two-stage analysis provides a useful test of whether the calibration framework remains reliable when the data are perturbed.

Figure 4 presents the comparison between the synthetic true trajectories and the corresponding fitted trajectories for all state variables of the model. It is observed that the fitted curves closely follow the reference solutions for all compartments, showing that the calibration procedure is able to reproduce the main temporal patterns of the epidemic system. In particular, the agreement is very strong for the susceptible, exposed, mild infected, severe infected, carrier, treated, recovered, and environmental bacteria classes, which indicates that the estimation framework successfully captures the dominant interactions among transmission, treatment, relapse, and environmental contamination.

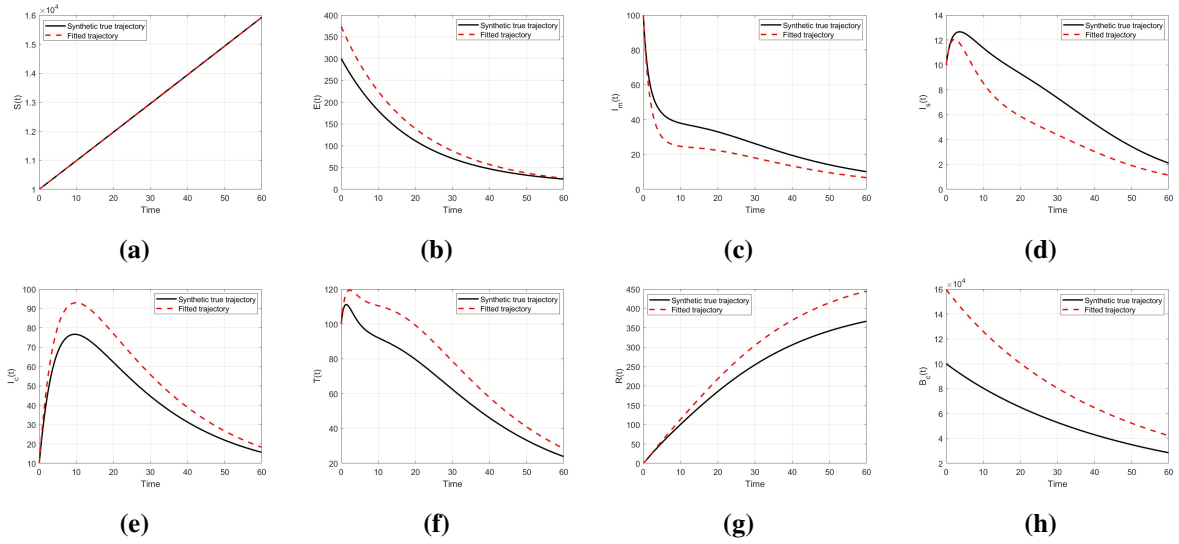


**Figure 4.** Comparison between the synthetic true trajectories and the corresponding fitted trajectories for the state variables of the proposed typhoid fever model. The close agreement between the reference and fitted solutions confirms that the calibration procedure accurately reconstructs the main dynamical patterns of the system.

The large percentage error observed for $\beta_1$ deserves further comment. Although the fitted trajectories reproduce the overall epidemic patterns, accurate trajectory fitting does not necessarily guarantee accurate estimation of each individual parameter. In the present model, $\beta_1$ enters the direct-transmission part of the force of infection,

$$\lambda(t) = \beta_1 \frac{I_s + \alpha_1 I_m + \alpha_2 I_c}{N_h} + \beta_2 \frac{B_c}{K + B_c},$$

whereas the early infection dynamics are also influenced by $\beta_2$, $E(0)$, and $B_c(0)$. Hence, different combinations of these parameters may generate similar values of the total force of infection and consequently similar state trajectories. This compensatory behavior explains why the trajectory-level fit can remain satisfactory even when the recovered value of $\beta_1$ differs substantially from its reference value. Moreover, because the true value of $\beta_1$ is very small, even a moderate absolute deviation can produce a very large relative percentage error. Therefore, the present results suggest that $\beta_1$ is

practically weakly identifiable under the current synthetic-data configuration. However, this should not be interpreted as proof of structural unidentifiability, since a formal structural identifiability analysis is beyond the scope of the present work.

Figure 5 shows the fitting results when noisy synthetic observations are used instead of clean trajectories. As expected, the observed data exhibit visible fluctuations around the underlying epidemic trends. Nevertheless, the fitted trajectories still capture the global shape of the data and preserve the principal temporal behavior of each compartment. This confirms that the proposed estimation method is stable under moderate perturbations and is capable of extracting meaningful model dynamics even in the presence of observational noise.

To further investigate the variability of the calibrated dynamics, Figure 6 displays multiple virtual trajectories generated around the fitted solution. These trajectories provide an ensemble-type representation of the uncertainty surrounding the estimated model response. Although the realizations differ in amplitude and local variation, their overall trends remain consistent with the fitted solution, demonstrating that the calibrated model preserves structural stability across repeated simulations.

A more compact visualization of this uncertainty is given in Figure 7, where the mean fitted trajectory is plotted together with ±1 standard deviation bands for each state variable. The shaded bands quantify the dispersion of the virtual trajectories around the mean solution. It can be seen that the uncertainty is relatively small for some compartments and more pronounced for others, especially in phases where the system changes rapidly. These plots provide additional confidence that the calibrated model not only reproduces the central epidemic trend but also offers a reasonable description of variability in the fitted dynamics.

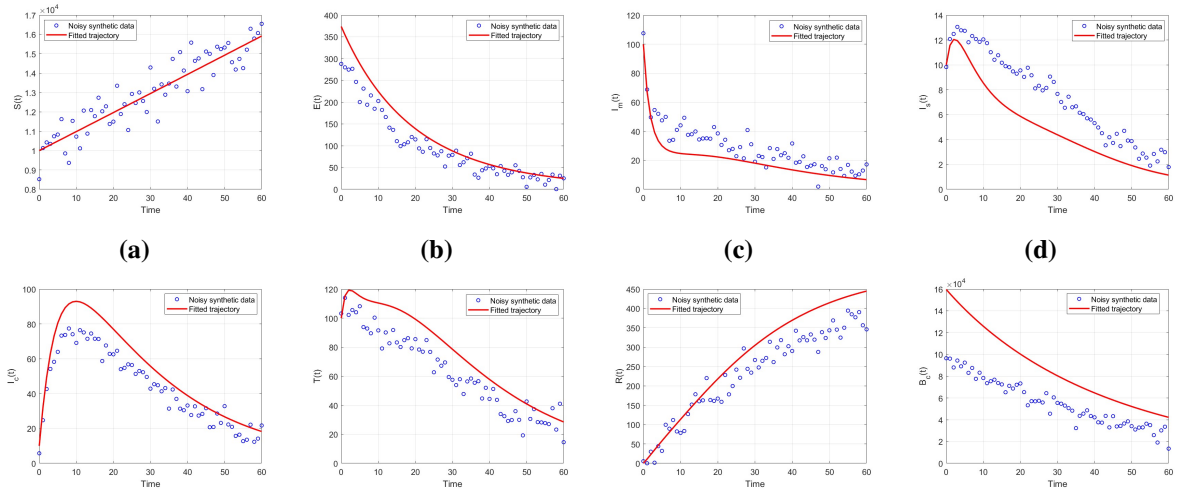


**Figure 5.** Comparison between noisy synthetic observations and the fitted trajectories for the state variables of the proposed typhoid fever model. The fitted curves capture the main trends of the noisy data, indicating the robustness of the parameter estimation procedure in the presence of measurement perturbations.

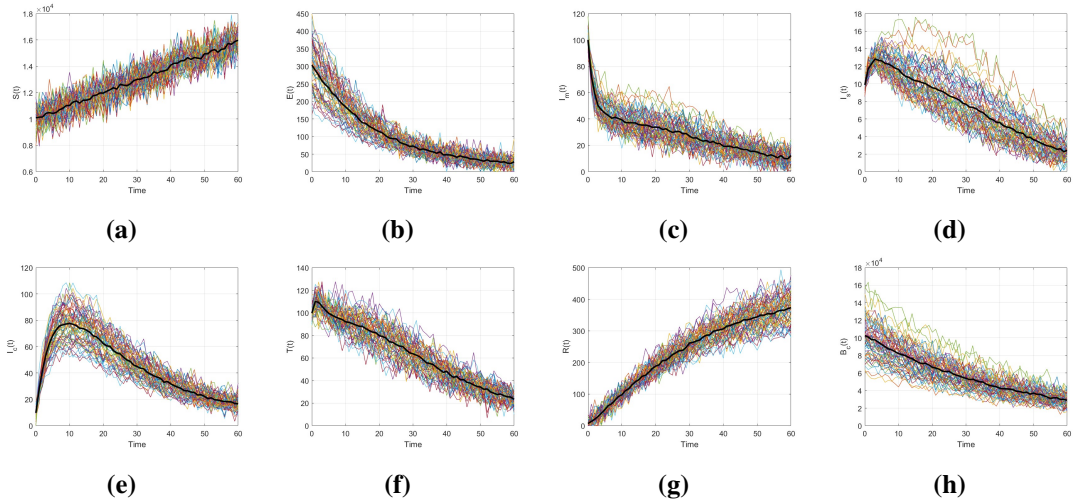


**Figure 6.** Multiple virtual trajectories generated around the fitted solution for the state variables of the proposed typhoid fever model. The ensemble of trajectories reflects variability in the simulated dynamics, while the central trend highlights the dominant temporal behavior of each compartment.

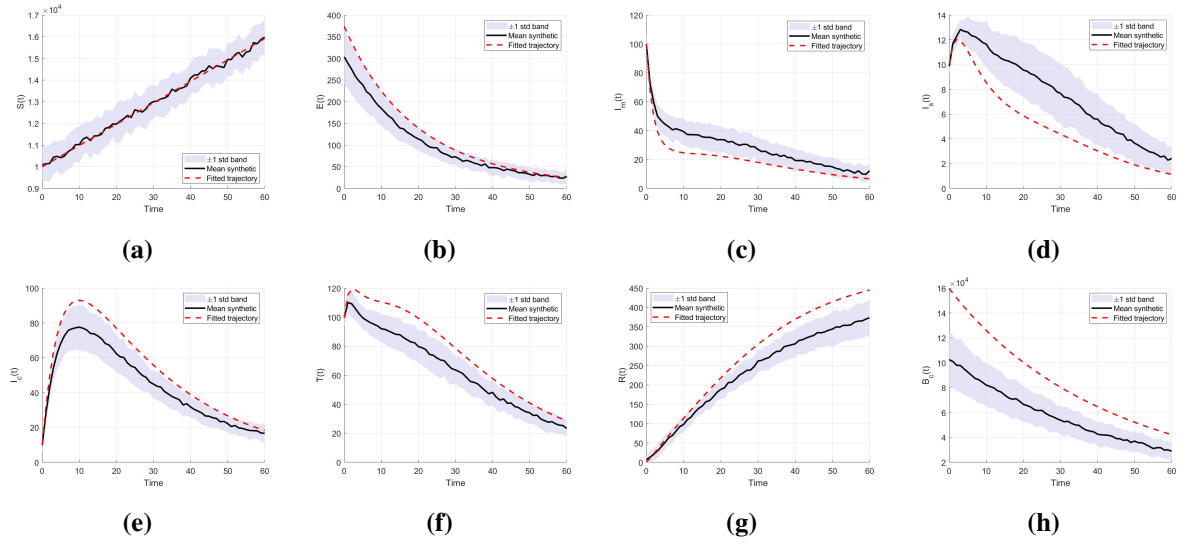


**Figure 7.** Mean fitted trajectories with ±1 standard deviation bands for the state variables of the proposed typhoid fever model. The shaded regions quantify the dispersion of the virtual trajectories around the mean solution and provide a visual summary of the uncertainty in the fitted dynamics.

Figure 8 provides heatmap representations of the normalized clean trajectories, normalized fitted trajectories, and normalized absolute error. The first two heatmaps show very similar temporal patterns across the model compartments, while the absolute-error heatmap indicates that the fitting errors remain concentrated in relatively low ranges across the simulation window. This visual agreement supports the conclusion that the calibrated model is able to recover the main structure of the synthetic epidemic data in a consistent manner.

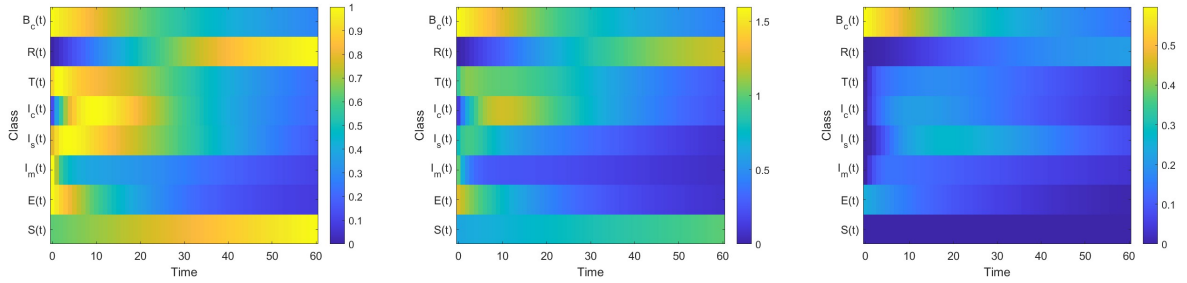


**(a)** **(b)** **(c)**

**Figure 8.** Heatmap representation of trajectory patterns for the proposed typhoid fever model: (a) normalized clean trajectories, (b) normalized fitted trajectories, and (c) normalized absolute error. The maps summarize the temporal variation across all model compartments and highlight the overall agreement between the reference and fitted solutions.

The numerical values of the estimated parameters are summarized in Table 1, together with the corresponding absolute and percentage errors. The results show that some parameters are recovered with relatively good accuracy, while others exhibit larger deviations from their true values. In particular, $\tau_3$, $\theta_2$, $\varpi_2$, $E(0)$, and $B_c(0)$ are estimated with moderate error levels, whereas the relative error in $\beta_1$ is large. This behavior suggests that certain parameters may be more practically identifiable than others under the available data configuration. Even so, the trajectory-level fits in Figures 4–8 remain satisfactory in reproducing the main dynamical patterns, although the large error in $\beta_1$ indicates that good trajectory reconstruction does not necessarily imply reliable recovery of every individual parameter.

The results of this section demonstrate that the proposed calibration framework provides a reliable way to estimate important transmission- and treatment-related quantities in the typhoid fever model. The fitted solutions remain in close agreement with both clean and noisy synthetic data, the uncertainty analysis confirms the stability of the calibrated trajectories, and the heatmap comparison further illustrates the consistency between the reference and estimated dynamics. Therefore, the parameter estimation procedure offers a solid foundation for subsequent prediction, sensitivity analysis, and data-driven surrogate modeling of the proposed fractional typhoid fever system.

## 8. Conclusions

This study introduced and analyzed a fractional-order typhoid fever model that incorporates treatment relapse and environmental bacterial contamination through the mABC derivative. The model was designed to represent the principal epidemiological features of the disease, including direct transmission, indirect infection through the environment, treatment dynamics, relapse after treatment, and bacterial shedding. The theoretical analysis verified key properties of the system, namely positivity, boundedness, existence, and uniqueness of solutions, showing that the model is both mathematically reliable and biologically admissible. To investigate the dynamics of the system, an approximate recursive solution was derived by applying the LADM. The resulting numerical experiments, carried out for several fractional-order values, revealed that memory effects play an important role in shaping the transient behavior of all compartments. In particular, variations in the

fractional order were found to alter the temporal profiles of the susceptible, exposed, mild infected, severe infected, carrier, treated, recovered, and environmental bacterial populations, while preserving nonnegative and epidemiologically meaningful trajectories. On the computational side, a DNN surrogate was trained using the numerically generated solutions in order to approximate the model outputs efficiently. The performance measures obtained from training, validation, testing, regression, and error analysis indicated that the surrogate model reproduced the simulated trajectories with high accuracy. In addition, a calibration procedure based on clean and noisy synthetic observations was implemented to estimate selected parameters and assess the robustness of the fitted solutions. The resulting fitted trajectories, uncertainty bands, and heatmap visualizations showed satisfactory agreement with the reference dynamics. The proposed framework offers a comprehensive approach for examining typhoid fever dynamics in the presence of relapse, treatment effects, and environmental contamination. By combining fractional-order modeling, decomposition-based approximation, neural-network surrogates, and parameter calibration, the study provides a useful foundation for future work on prediction, sensitivity analysis, and data-driven epidemiological assessment. A limitation of the calibration results is that some parameters, especially $\beta_1$, appear to be practically weakly identifiable under the present synthetic-data setting. Future work will include formal structural and practical identifiability analysis, profile-likelihood assessment, and calibration using richer observational data to improve the reliability of individual parameter estimates.

## Author contributions

Ramsha Shafqat: Conceptualization, Methodology, Software, Formal analysis, Investigation, Resources, Writing–original draft, Writing–review and editing, Supervision; Mohammed M. Alshamrani: Software, Investigation, Resources, Project administration, Funding acquisition. All authors have read and approved the final version of the manuscript for publication.

## Use of Generative-AI tools declaration

The authors declare they have not used Artificial Intelligence (AI) tools in the creation of this article.

## Acknowledgments

The authors would like to acknowledge the Deanship of Graduate Studies and Scientific Research, Taif University for funding this work.

## Conflict of interest

All authors declare no conflicts of interest in this paper.

## References

1. S. Mushayabasa, C. P. Bhunu, E. T. Ngarakana-Gwasira, Mathematical analysis of a typhoid model with carriers, direct and indirect disease transmission, *International J. Math. Sci. Eng. Appl.*, **7** (2013), 79–90.

2. World Health Organization, Typhoid vaccines: WHO position paper–March 2018, *Weekly Epidemiological Record*, **93** (2018), 153–172.
3. G. T. Tilahun, O. D. Makinde, D. Malonza, Modelling and optimal control of typhoid fever disease with cost-effective strategies, *Comput. Math. Meth. Med.*, **2017** (2017), 2324518. https://doi.org/10.1155/2017/2324518
4. M. K. Bhan, R. Bahl, S. Bhatnagar, Typhoid and paratyphoid fever, *Lancet*, **366** (2005), 749–762. https://doi.org/10.1016/S0140-6736(05)67181-4
5. World Health Organization, Typhoid vaccines: WHO position paper, *Weekly Epidemiological Record*, **83** (2008), 49–59.
6. A. K. Schemmer, Heterogeneity of inflammation and host metabolism in a thyphoid fever model, PhD diss., Verlag nicht ermittelbar, 2012.
7. T. Butler, Treatment of typhoid fever in the 21st century: Promises and shortcomings, *Clin. Microbiol. Infect.*, **17** (2011), 959–963.https://doi.org/10.1111/j.1469-0691.2011.03552.x
8. K. A. Tijani, C. E. Madubueze, R. I. Gweryina, Modelling typhoid fever transmission with treatment relapse response: Optimal control and cost-effectiveness analysis, *Math. Models Comput. Simul.*, **16** (2024), 457–485. https://doi.org/10.1134/S2070048224700169
9. B. A. Connor, E. Schwartz, Typhoid and paratyphoid fever in travellers, *Lancet Infect. Dis.*, **5** (2005), 623–628. https://doi.org/10.1016/S1473-3099(05)70239-5
10. R. B. Kiplang'at, W. Kirui, L. O. Olwamba, B. Tonui, Prey-predator model on the interaction of pathogenic bacteria and bacteriophages in the presence of medication, *J. Adv. Math. Comput. Sci.*, **39** (2024), 71–84. https://doi.org/10.9734/jamcs/2024/v39i91928
11. H. Abboubakar, R. Racke, Mathematical modeling, forecasting, and optimal control of typhoid fever transmission dynamics, *Chaos Solitons Fract.*, **149** (2021), 111074. https://doi.org/10.1016/j.chaos.2021.111074
12. I. Petráš, *Fractional-order nonlinear systems: Modeling, analysis and simulation*, Berlin: Springer Science & Business Media, 2011.
13. P. Okolo, O. Abu, On optimal control and cost-effectiveness analysis for typhoid fever model, *Fudma J. Sci.*, **4** (2020), 437–445. https://doi.org/10.33003/fjs-2020-0403-258
14. I. Podlubny, *Fractional differential equations: An introduction to fractional derivatives, fractional differential equations, to methods of their solution and some of their applications*, Amsterdam: Elsevier, 1998.
15. A. Zeb, G. Nazir, K. Shah, E. Alzahrani, Theoretical and semi-analytical results to a biological model under Atangana–Baleanu–Caputo fractional derivative, *Adv. Diff. Equ.*, **2020** (2020), 654. https://doi.org/10.1186/s13662-020-03117-7
16. C. Milici, G. Drăgănescu, J. T. Machado, *Introduction to fractional differential equations*, Berlin: Springer, 2018.
17. M. N. Jan, T. Khan, G. Zaman, Analytical approximate solution of hepatitis B epidemic model comparison with vaccination, *Punjab Uni. J. Math.*, **51** (2019), 53–69.
18. A. I. Abioye, M. O. Ibrahim, O. J. Peter, S. Amadiegwu, F. A. Oguntolu, Differential transform method for solving mathematical model of SEIR and SEI spread of malaria, Verlag nicht ermittelbar, 2018.

19. A. Ahmad, R. Ali, I. Ahmad, F. A. Awwad, E. A. Ismail, Global stability of fractional order HIV/AIDS epidemic model under caputo operator and its computational modeling, *Fractal Fract.*, **7** (2023), 643. https://doi.org/10.3390/fractalfract7090643
20. A. Ahmad, R. Ali, I. Ahmad, M. Ibrahim, Fractional view analysis of the transmission dynamics of norovirus with contaminated food and water, *Int. J. Biomath.*, **17** (2024), 2350072. https://doi.org/10.1142/S1793524523500729
21. R. Ali, Z. Zhang, H. Ahmad, M. M. Alam, The analytical study of soliton dynamics in fractional coupled Higgs system using the generalized Khater method, *Opt. Quant. Electron.*, **56** (2024), 1067. https://doi.org/10.1007/s11082-024-06924-4
22. R. Ali, Z. Zhang, H. Ahmad, Exploring soliton solutions in nonlinear spatiotemporal fractional quantum mechanics equations: an analytical study, *Opt. Quant. Electron.*, **56** (2024), 838. https://doi.org/10.1007/s11082-024-06370-2
23. A. Al-Quran, R. Shafqat, A. Alsaadi, A. M. Djaouti, Well-posedness and ulam–Hyers stability of a normalized Caputo–Fabrizio fractional model for ischemic heart disease progression, *J. Math.*, **2026** (2026), 9509503. https://doi.org/10.1155/jom/9509503
24. R. Shafqat, K. Abuasbeh, S. Trabelsi, M. Balti, Epidemic dynamics prediction using fractional SIRD and deep learning, *Sci. Rep.*, **16** (2025), 3043. https://doi.org/10.1038/s41598-025-34299-3
25. R. Shafqat, Imran, A. Al-Quran, A. M. Djaouti, Enhancing rabies epidemic modeling with neural networks and fractional calculus, *Sci. Rep.*, **16** (2026), 10409. https://doi.org/10.1038/s41598-026-40853-4
26. A. Al-Quran, R. Shafqat, A. Alsaadi, A. M. Djaouti, A hybrid fractal-fractional and machine learning framework for Zika virus spread prediction, *J. Math.*, **2026** (2026), 9999891. https://doi.org/10.1155/jom/9999891
27. S. M. Alamry, R. Shafqat, A. Alsaadi, Poliomyelitis dynamics under the normalized caputo–fabrizio operator: Analysis, stability, and numerics, *J. Taibah Uni. Sci.*, **20** (2026), 2659460. https://doi.org/10.1080/16583655.2026.2659460
28. T. Li, S. Frassu, G. Viglialoro, Combining effects ensuring boundedness in an attraction-repulsion chemotaxis model with production and consumption, preprint paper, 2022. https://doi.org/10.48550/arXiv.2211.03608
29. T. Li, D. Acosta-Soba, A. Columbu, G. Viglialoro, Dissipative gradient nonlinearities prevent $\delta$-formations in local and nonlocal attraction–repulsion chemotaxis models, *Stud. Appl. Math.*, **154** (2025), e70018. https://doi.org/10.1111/sapm.70018
30. J. Mushanyu, F. Nyabadza, G. Muchatibaya, P. Mafuta, G. Nhawu, Assessing the potential impact of limited public health resources on the spread and control of typhoid, *J. Math. Biol.*, **77** (2018), 647–670. https://doi.org/10.1007/s00285-018-1219-9
31. S. Rashid, A. A. El-Deeb, M. Inc, A. Akgül, M. Zakarya, W. Weera, Stochastic dynamical analysis of the co-infection of the fractional pneumonia and typhoid fever disease model with cost-effective techniques and crossover effects, *Alex. Eng. J.*, **69** (2023), 35–55. https://doi.org/10.1016/j.aej.2023.01.027
32. H. Abboubakar, R. K. Regonne, K. S. Nisar, Fractional dynamics of typhoid fever transmission models with mass vaccination perspectives, *Fractal Fract.*, **5** (2021), 149. https://doi.org/10.3390/fractalfract5040149

33. M. Al-Refai, D. Baleanu, On an extension of the operator with Mittag-Leffler kernel, *Fractals*, **30** (2022), 2240129. https://doi.org/10.1142/S0218348X22401296
34. I. A. Adetunde, Mathematical models for the dynamics of typhoid fever in kassena-nankana district of upper east region of Ghana, *J. Mod. Math. Stat.*, **2** (2008), 45–49.
35. J. M. Mutua, F. B. Wang, N. K. Vaidya, Modeling malaria and typhoid fever co-infection dynamics, *Math. Biosci.*, **264** (2015), 128–144. https://doi.org/10.1016/j.mbs.2015.03.014
36. H. R. Amick, Typhoid and paratyphoid fever, In: *CDC Yellow Book 2020: Health Information for International Travel*, **177** (2019), 364.
37. M. Ghosh, P. Chandra, P. Sinha, J. B. Shukla, Modelling the spread of bacterial infectious disease with environmental effect in a logistically growing human population, *Nonlinear Anal.: Real World Appl.*, **7** (2006), 341–363. https://doi.org/10.1016/j.nonrwa.2005.03.005
38. K. A. Tijani, C. E. Madubueze, R. I. Gweryina, Typhoid fever dynamical model with cost-effective optimalcontrol, *J. Niger. Soc. Phys. Sci.*, **5** (2023), 1579. https://doi.org/10.46481/jnsps.2023.1579


AIMS Press